UNIVERSITY OF LEEDS

This is a repository copy of *Imaging of a distinctive large bubble in gas-water flow based on size projection algorithm*.

White Rose Research Online URL for this paper:
http://eprints.whiterose.ac.uk/149073/

Version: Accepted Version

**Article:**
Li, K, Wang, Q, Wang, M orcid.org/0000-0003-0941-8481 et al. (1 more author) (2019) Imaging of a distinctive large bubble in gas-water flow based on size projection algorithm. Measurement Science and Technology, 30 (9). 094004. ISSN 0957-0233

https://doi.org/10.1088/1361-6501/ab16b0

(c) 2019, IOP Publishing Ltd. This manuscript version is made available under the CC-BY-NC-ND 3.0 license https://creativecommons.org/licenses/by-nc-nd/3.0/

**Reuse**
This article is distributed under the terms of the Creative Commons Attribution-NonCommercial-NoDerivs (CC BY-NC-ND) licence. This licence only allows you to download this work and share it with others as long as you credit the authors, but you can't change the article in any way or use it commercially. More information and the full terms of the licence here: https://creativecommons.org/licenses/

**Takedown**
If you consider content in White Rose Research Online to be in breach of UK law, please notify us by emailing eprints@whiterose.ac.uk including the URL of the record and the reason for the withdrawal request.

White Rose university consortium
Universities of Leeds, Sheffield & York

eprints@whiterose.ac.uk
https://eprints.whiterose.ac.uk/

Measurement Science and Technology

**ACCEPTED MANUSCRIPT**

# Imaging of a distinctive large bubble in gas-water flow based on size projection algorithm

To cite this article before publication: Kun Li *et al* 2019 *Meas. Sci. Technol.* in press https://doi.org/10.1088/1361-6501/ab16b0

Manuscript version: Accepted Manuscript

Accepted Manuscript is "the version of the article accepted for publication including all changes made as a result of the peer review process, and which may also include the addition to the article by IOP Publishing of a header, an article ID, a cover sheet and/or an 'Accepted Manuscript' watermark, but excluding any other editing, typesetting or other changes made by IOP Publishing and/or its licensors"

This Accepted Manuscript is **© 2019 IOP Publishing Ltd**.

During the embargo period (the 12 month period from the publication of the Version of Record of this article), the Accepted Manuscript is fully protected by copyright and cannot be reused or reposted elsewhere.
As the Version of Record of this article is going to be / has been published on a subscription basis, this Accepted Manuscript is available for reuse under a CC BY-NC-ND 3.0 licence after the 12 month embargo period.

After the embargo period, everyone is permitted to use copy and redistribute this article for non-commercial purposes only, provided that they adhere to all the terms of the licence https://creativecommons.org/licences/by-nc-nd/3.0

Although reasonable endeavours have been taken to obtain all necessary permissions from third parties to include their copyrighted content within this article, their full citation and copyright line may not be present in this Accepted Manuscript version. Before using any content from this article, please refer to the Version of Record on IOPscience once published for full citation and copyright details, as permissions will likely be required. All third party content is fully copyright protected, unless specifically stated otherwise in the figure caption in the Version of Record.

View the article online for updates and enhancements.

This content was downloaded from IP address 129.11.112.113 on 03/07/2019 at 11:41

**IOP** Publishing Journal Title
Journal **XX** (XXXX) XXXXXX https://doi.org/XXXX/XXXX

# Imaging of a distinctive large bubble in gas-water flow based on size projection algorithm

**Kun Li[1,2], Qiang Wang[2], Mi Wang[2,*] and Yan Han[1]**

[1] Shanxi Key Lab of Signal Capturing & Processing, North University of China, Taiyuan, 030051, China
[2] School of Chemical and Process Engineering, University of Leeds, Leeds, LS2 9JT, UK

E-mail: m.wang@leeds.ac.uk

Received xxxxxx
Accepted for publication xxxxxx
Published xxxxxx

## Abstract

Although electrical resistance tomography has been successfully applied to visualise gas-water two-phase flow in many applications, its capability on determination of the sharp interfaces between gas bubble and water is still under the engineering expectation, which impedes effective estimating of fluid characteristics and flow regimes. Thresholding value method applied to tomogram was demonstrated a splendid view to most flow regimes, especially a large bubble but may present a challenge on its correctness in practice since the thresholding value was determined empirically. In this paper, a size projection algorithm is proposed for imaging a large bubble with distinctive boundary, where the optimal thresholding value is automatically determined by minimising the projection error between measured voltages and computed voltages via a forward numerical solution, which specifically focuses on imaging of large bubble. The accuracy of imaging large bubble is evaluated by simulating the typical cross-sectional configurations of common pipeline flow regimes. Experimental results are reported in the paper, which were conducted on both horizontal and vertical pipelines engaged with typical gas-water flow regimes, including stratified, plug, slug and annular flow regimes. The results are also compared with the images obtained from wire-mesh sensor system and high-speed camera videos recorded through a transparent photo-chamber lined in the test rig.

Keywords: electrical resistance tomography, gas-water flow, distinctive large bubble, thresholding value, projection error minimisation.

## 1. Introduction

Gas-liquid two-phase flow is a common and important process in many industries, where the measuring of flow parameters for understanding flow dynamics in process equipment is of significance for operation, analysis and design of these equipment [1,2]. Large and growing of researches have been conducted to develop robust and effective techniques for gas-liquid flow measurement and visualisation in the past, which can be categorised by invasive and non-invasive techniques [3,4,5]. Due to electrical resistance tomography (ERT) offering a non-intrusive and cost-effective solution with a high temporal resolution (sub-millisecond) [6], it has been successfully applied to gas-liquid two-phase applications. However, it is normally incapable for determining sharp gas-liquid interfaces because of its relatively low spatial resolution (up to 5%) [2], which impedes effectively characterizing and visualising of gas-liquid two-phase flows.

Thresholding value methods, a kind of image segmentation method, were successfully applied to enhance the effectiveness of visualisation for gas-liquid flow, which demonstrated a splendid view to most flow regimes, especially

Accepted Manuscript

 © xxxx IOP Publishing Ltd

for a distinctive large bubble. The thresholding value method is simple but the determination of thresholding value in the methods is based on engineering experience or empirical results. Wang [7,8] utilised a fixed empirical value to estimate the air-core size in a separator, and Xie [9] and Yan [10] employed a pre-set multiplication coefficient obtained from simulation and mean reconstructed value as thresholding value for objects extraction. These kinds of threshold value selection are often arbitrary, and may not be adaptive and optimal for other cases. Some histogram-based methods were also proposed for selecting of threshold value with various model-fitting methods [11,12]. The histogram was used as the basic selection criterion to automatically select optimal threshold by modelling histogram curve as Gaussian mixtures model [13], maximising the entropy of histogram, or maximising the separability of resultant classes in grey levels [14,15]. However, the histograms of reconstructed images do not often fit a clear model well in practice, and the reconstructed images may be polluted by artifacts noise due to limited projection data and unavoidable measurement noise.

In this paper, a size projection algorithm is proposed for imaging a large bubble with distinctive boundary, where the optimal thresholding value is automatically determined by minimising the projection error between measured voltages and computed voltages via a forward numerical solution, which specifically focuses on imaging of large bubble. Simulation is conducted for evaluating the accuracy of imaging large bubble based on the typical cross-sectional configurations of most flow regimes. Then, results are reported for visualisation of typical flow regimes in both horizontal and vertical pipelines with 50mm-diameter, including stratified, plug, slug and annular flow regimes. The results are also compared with high-speed camera videos recorded through a transparent photo-chamber and images obtained from wire-mesh sensor (WMS) system.

## 2. Methodology

Considering fully developed gas-water flows in both horizontal and vertical pipelines [1,16], the gas distributions can be characterized as three cases of (1) small bubbles (e.g. bubbly regime), or (2) only a large bubble (e.g. stratified, slug, plug or annular regimes), or (3) a large bubble with few small bubbles in its tail (e.g. slug or plug regimes). According to bubble merging principle [17,18], the large bubble is main part in the determining of gas void fraction. In general, the large bubbles, if exist, also play a dominant role in tomographic imaging, and the influence from small bubbles is mostly depressed in tomograms since they are normally few accompanied with a large bubble in these typical flow regimes. Therefore, the reconstructed tomographic flow regimes of developed pipeline flows may be approximated as either a large bubble or small bubbles without the loss of flow regime features. This approximation makes the proposed method feasible for visualisation of flow regimes in developed pipeline flows. With the ignoring of small bubbles in the case (3), the size projection-based algorithm was proposed for extracting gas-water interface of large bubbles, which may also enhance the visualisation performance of distinctive bubble in stated flow cases of (2) and (3).

### 2.1 Size projection algorithm

The thresholding value methods, such as the empirical-based or histogram-based methods, work well for approximate visualisation of gas-water two-phase flow, but would be struggled in its precision in identification of large bubble size. To improve the precision of bubble size, the multistep image segmentation is utilised to determine an accurate threshold for imaging large bubble. The procedure of forward solution has to be employed to compute the boundary data of segmented bubble, and a projection error, that is the difference between measured boundary data and computed boundary data, is generated as threshold selection criterion.

#### 2.1.1 Formulation of projection error function.

Referring to the error concept in error function decomposition method [20], the equation (1) is used to represent the projection error.

$$e_j^{(p)} = \frac{V_j'(\sigma')}{V_j(\sigma_0)} - \frac{u_j'(\hat{\sigma}_k^{(p)})}{u_j(\hat{\sigma}_k^{(0)})} \qquad (1)$$

where, $e_j^{(p)}$ is the projection error at projection j with respect to the p-th step segmentation. $V_j(\sigma_0)$ and $V_j'(\sigma')$ are the measured reference voltage and measurement voltage, i.e. measured boundary projection data. $u_j(\hat{\sigma}_k^{(0)})$ and $u_j'(\hat{\sigma}_k^{(p)})$ are the computed reference voltage and measurement voltage with respect to the conductivity distribution $\hat{\sigma}_k^{(0)}$ and $\hat{\sigma}_k^{(p)}$, i.e. computed boundary data from forward solution. j and k refer to the projection number and the pixel number of finite mesh, respectively. The equation (1) transforms the relative change of measurement domain to a simulation domain, which significantly reduces the error effects from measurement noise, electrodes inconsistency and field dimensions [21].

The error function of in the error function decomposition method was used to evaluate the approximation of nonlinear inverse solution in literature [20]. However, the concept of error evaluation is employed to represent the projection error due to the effect of thresholding value's difference for evaluating the similarity between segmented bubble distribution and real bubble distribution in this paper, where the projection error should reach its minimal if the segmented bubble is close to the real one.

Given a measured field $\boldsymbol{\varphi}_N$ with respect to a finite mesh in N-pixels, and a reconstructed concentration set $\boldsymbol{C}$ over $\boldsymbol{\varphi}_N$ (i.e. gas concentration tomogram), the concentration values are defined as

Accepted Manuscript

$$\boldsymbol{C} = \{c_k\},\ \mathrm{k}=1, 2,\ldots, \mathrm{N} \quad (2)$$

Due to unavoidable noise from measurement and image reconstruction, the concentration set may contain some abnormal data, e.g. negative values. Therefore, the data set have to be filtered first to fit the meaningful concentration range, i.e. [0.0,1.0]. A simple filter is defined by

$$\mathrm{F}(c_k) = \begin{cases} 0.0 & c_k < 0 \\ c_k & 0 \le c_k \le 1 \\ 1.0 & c_k > 1 \end{cases} \quad (3)$$

Then, let a thresholding value, $x \in [0.0,1.0]$, employed to convert the reconstructed concentration set $\boldsymbol{C}$ (corresponding to a blurry image) to a binary concentration set $\hat{\boldsymbol{C}}$ (corresponding to an image in which gas bubble-water interface having a sharp boundary), as expressed by

$$\hat{c}_k = \begin{cases} 0.0 & c_k < x \\ 1.0 & c_k \ge x \end{cases} \quad (4)$$

Equation (4) describes that the k-th pixel is fully occupied by gas if gas concentration value beyond the given threshold $x$, and otherwise it is occupied by water. By introducing the conductivity of dispersed gas phase (i.e. 0 S/m) and the conductivity of continuous water phase (i.e. reference conductivity, $\sigma_0$), the conductivity vector $\hat{\boldsymbol{\sigma}}$ of segmented image can be obtained with filling water conductivity into water occupied pixels and filling gas conductivity into gas occupied pixels, which is expressed by

$$\hat{\sigma}_k = \begin{cases} 0 & c_k = 1.0 \\ \sigma_0 & c_k = 0.0 \end{cases} \quad (5)$$

For the binary conductivity distribution vector $\hat{\boldsymbol{\sigma}}$ with respect to the threshold $x$, the forward solution can be approximately represented by the finite element method (FEM) model, which can be solved by the following linear equations [22,23]

$$\boldsymbol{Y}\boldsymbol{v} = \boldsymbol{c} \quad (6)$$

where, $\boldsymbol{Y}$ is the admittance matrix with respect to the segmented conductivity distribution vector $\hat{\boldsymbol{\sigma}}$, and $\boldsymbol{v}$ is the nodal voltage vector for obtaining the computed boundary data $\mathbf{u}'(\hat{\boldsymbol{\sigma}})$, and $\boldsymbol{c}$ is the nodal current vector. Since the admittance matrix $\boldsymbol{Y}$ has been proven as a $N \times N$ symmetrical and positively defined matrix [24], the equation (6) can be solved by conjugate gradient (CG) method. The CG method employs the idea of minimising the constructed function $f(\boldsymbol{v}) = \frac{1}{2}\boldsymbol{v}\boldsymbol{Y}\boldsymbol{v} - \boldsymbol{c}\boldsymbol{v}$ through up to N iterations of conjugate directions $\boldsymbol{p}$. Let initial nodal voltage vector as $\boldsymbol{v_0}$ and calculate the initial searching direction $\boldsymbol{p_0}$, as given by

$$\boldsymbol{v_0} = \left(v_1^{(0)}, v_2^{(0)}, \ldots, v_N^{(0)}\right)^T = (0,0,\ldots,0)^T \quad (7)$$

$$\boldsymbol{p_0} = \boldsymbol{r_0} = \boldsymbol{c} - \boldsymbol{Y}\boldsymbol{v_0} \quad (8)$$

Carry out the iterations from $i = 0$ to $N-1$ with the following equations (9)-(13), until the residual $\boldsymbol{r_i}$ is enough small

$$\alpha_i = \frac{\boldsymbol{r_i^T}\boldsymbol{r_i}}{\boldsymbol{p_i^T}\boldsymbol{Y}\boldsymbol{p_i}} \quad (9)$$

$$\boldsymbol{v_{i+1}} = \boldsymbol{v_i} + \alpha_i \boldsymbol{p_k} \quad (10)$$

$$\boldsymbol{r_{i+1}} = \boldsymbol{r_i} - \alpha_i \boldsymbol{Y}\boldsymbol{p_k} \quad (11)$$

$$\beta_i = \frac{\boldsymbol{r_{i+1}^T}\boldsymbol{r_{i+1}}}{\boldsymbol{r_i^T}\boldsymbol{r_i}} \quad (12)$$

$$\boldsymbol{p_{i+1}} = \boldsymbol{r_{i+1}} - \beta_i \boldsymbol{p_k} \quad (13)$$

After the above procedures, the approximate solution of nodal voltage vector $\boldsymbol{v}$ is reached, and the computed boundary voltage vector $\boldsymbol{u}'(\hat{\boldsymbol{\sigma}})$ with respect to the threshold $x$ can be obtained by following a specific sensing strategy (adjacent sensing strategy is used in this paper, i.e. 104 independent measurements).

Following equation (1), the projection error vector $\boldsymbol{e}$ corresponding to the threshold $x$ is calculated. With adjusting the threshold $x$, the converted binary conductivity vector $\hat{\boldsymbol{\sigma}}$, the computed boundary voltage vector $\boldsymbol{u}'(\hat{\boldsymbol{\sigma}})$, and the projection error vector $\boldsymbol{e}$ vary. Given a definition domain [0.0,1.0] relative to the range of gas concentration values, the projection error function of threshold is defined as the formulation

$$\boldsymbol{e} = F(x) \quad x \in [0.0,1.0] \quad (14)$$

where, the $F(x)$ maps a threshold $x$ to a projection error $\boldsymbol{e}$.

### 2.1.2 Threshold selection by minimising projection error.

Following the definition of projection error (equation (1)), the minimum of projection error means the closest size of the bubble in segmented image to the real one. Therefore, equation (14) transforms the threshold selection problem to optimisation problem of minimising projection error, as expressed by

$$\min \quad F(x), \quad s.t. \quad x \in [0.0,1.0] \quad (15)$$

Subjecting to the definition domain [0.0,1.0], formulation (15) belongs to nonlinear unconstrained optimization problem.

For an example in figure 1, a bubble is located at the centre of a circular vessel filled with water, and the gas concentration profile (i.e. blue curve in figure 1) contained artifacts was reconstructed, which could not reflect the bubble size but approximately maintain the bubble shape. Supposing a suitable thresholding cross-section with respect to threshold $x_c$, the grey shaded area at the thresholding cross-section should be similarly projected to that of real bubble in the vessel. However, the thresholds $x_a$ and $x_b$ underestimate and overestimate the size of real bubble, respectively. With adjusting the threshold from 0.0 to 1.0, the projected bubble size is firstly close to, and then deviate from the real bubble size, where the projection error function firstly decreases and then increases. Therefore, the projection error function is an unimodal function on threshold range [0.0,1.0].

Golden-section search (GS) method provides a general means of solving the optimization problem as expressed by the equation (15), since the threshold range [0.0,1.0] is a signal peak interval of $F(x)$. The detailed derivation of GS method can be found in literature [25]. However, the control factors in GS method are set with a minimum convergence error ε (i.e. measurement error) and maximum number of search steps $p$. The process of GS method is illustrated in the appendix A.1.

Accepted Manuscript

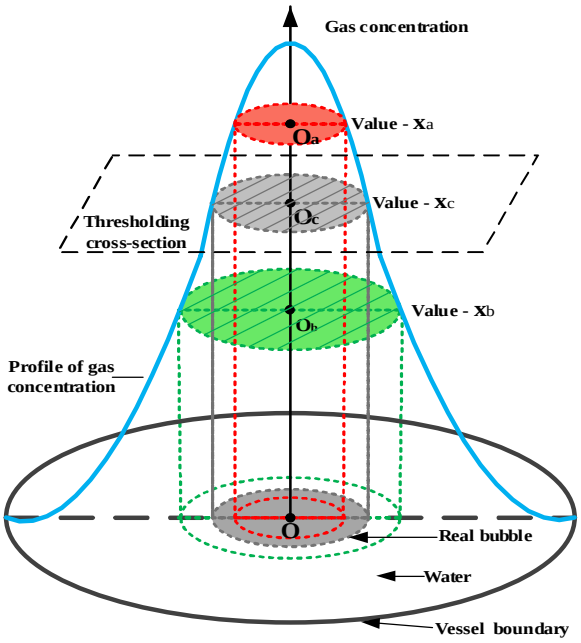


**Figure 1**. Segmentation process of the reconstructed bubble.

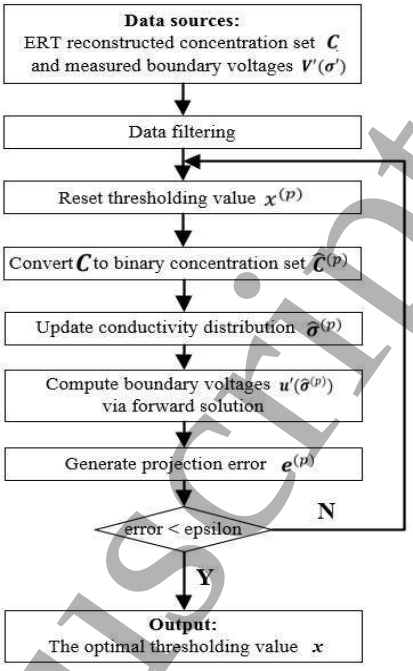


**Figure 2**. Flow chart of size projection algorithm.

By the application of GS method, the optimal threshold $x^{(p)}$ is automatically determined for the reconstructed concentration set $\boldsymbol{C}$. Meanwhile, the binary concentration set $\widehat{\boldsymbol{C}}^{(p)}$ in segmented image is obtained as well, where the segmented bubble size is colse to the real bubble size. As the optimal threshold value is determined by comparing the computed data of a sized projected bubble with the measured data of real bubble (i.e. minimising the projection error), the proposed tomographic image segmentation method is named as size projection algorithm.

The implementation procedures of size projection algorithm are illustrated in figure 2.

## 2.2 Visualisation of large bubble in gas-water flow

**2.2.1 Features extraction of gas-water flow.** As well known, ERT provides a cross-sectional visualisation solution for gas-water flow via reconstructing the conductivity tomogram $\boldsymbol{\sigma}'$ with a specific mesh. Then two vital parameters, gas concentration and axial velocity, can be derived from the reconstructed conductivity distribution $\boldsymbol{\sigma}'$ under the help of AIMFlow software [26].

Based on the simplified Maxwell relationship [19], the gas concentration tomogram can be derived by

$$c_{ERT} = \frac{2\sigma_0 - 2\sigma'}{\sigma_0 + 2\sigma'} \quad (16)$$

where, $\sigma_0$ is the conductivity of continuous water phase. $c_{ERT}$ and $\sigma'$ are the gas concentration and the reconstructed conductivity in each pixel, respectively. Then the local void fraction $\alpha_{ERT}$ can be expressed by the average of gas concentration in each pixel.

Because the real velocity field is hardly available from tomography-based methods, statistics-based methods, e.g. cross-correlation method, are employed to derive the axial velocity as an approximate gas velocity [27]. Given a dual-plane ERT system whose two parallel-installed electrode planes have a fixed interval, axial gas velocity can be derived with a direct pixel-to-pixel cross-correlation method by

$$R_{1,2}(n) = \sum_{m=n+1}^{N} f_1(m-n) \times f_2(m) \quad n = 0,1 \cdots N-1 \quad (17)$$

where, $f_i(m)$ is the $m$-th tomogram of $i$-th sensor plane. 1 and 2 in $R_{1,2}(n)$ are the number of the up-stream and down-stream sensor planes, $N$ is the image sampling length. Equation (17) is the general form of cross-section method for tomographic methods to seek for correlation [28], while its modified form in [29] is suitable for online calculation by updating $R_{1,2}(n)$ with the new $k$-th tomogram, which is expressed by

$$R_{1,2}^{k}(n) = R_{1,2}^{k-1}(n) + f_1(k-n) \times f_2(k) \quad n = 0,1 \cdots N-1 \quad (18)$$

The major different between (17) and (18) is that the former uses whole input tomograms to calculate mean pixel velocity distribution, whereas the latter does not, which leads to better results for latter equation. Therefore, the local gas velocity is approximated by equation (18) in this work.

It should be noted that due to the nature of certain flow regimes and cross-correlation principle, it is extremely difficult to extract the local gas velocity of these fluids by direct cross-correlation methods, such as horizontal stratified flow, annular flow and vertical annular flow. In this case, the superficial gas velocity is used to approximately estimate the real gas velocity in this work.

Accepted Manuscript

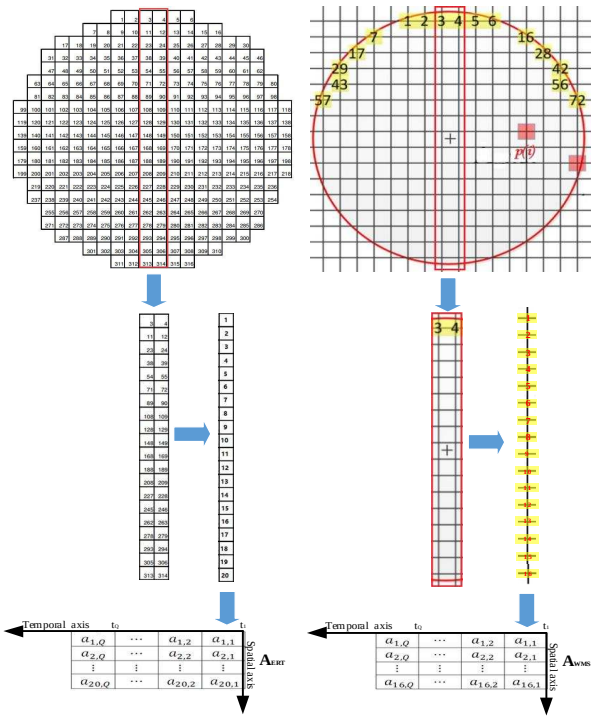


**Figure 3**. Generation process of axially-stacked sliced image.

Meanwhile, a wire-mesh sensor (WMS) also provides the cross-sectional visualisation solution for gas-water flow by measuring the local conductivity signal at each crossing-point of a specific fine wire-mesh [30]. Prasser [31] made a comparison between a 16*16 WMS and an ultra-fast X-ray CT on air-water pipeline fluid with different air-water rates, and the results from two modalities had a similar tendency on radial void fraction profile and a very good correspondence on average void fraction. Olerni [32] also made a comparison between a 16*16 WMS and a typical ERT on upwards air-water pipeline flow, and the results of two systems had a good coincidence even not exactly the same on gas void fraction. Therefore, a typical 16*16 WMS was installed at downside of ERT sensor for providing image reference to estimate the results of ERT and the proposed approach in this work.

The gas concentration set $\boldsymbol{C}_{WMS}$ from WMS can be derived by [30]

$$c_{WMS} = 1 - \frac{U^{meas}}{U^{W}} \tag{19}$$

where, $c_{WMS}$ is the local gas concentration (i.e. void fraction) at each crossing-point. $U^{W}$ and $U^{meas}$ are the time averaged sensor signal of a calibration measurement (tap water in this paper) and the local instantaneous sensor signal of the measured value, respectively. Then the local void fraction $\alpha_{WMS}$ can be expressed by the average of gas concentration at each crossing-point.

### 2.2.2 Visualisation of large bubble in gas-water flow.

As the horizontal gas-water flow may be assumed as symmetrical along a vertical axial plane, and the vertical flow may be assumed as symmetrical along the axial of pipeline, the axially-stacked central data columns of tomograms can supply a 2D view of gas-water flow in both spatial and temporal terms. Let $\boldsymbol{C}^i = \left\{ c_k^i \middle| k \in \{1,2,\ldots,N\} \right\}$ denotes the gas concentration sets obtained from ERT system or WMS system, where $i$ is the frame number of gas concentration set, and $N$ is the total number of ERT-mesh pixels or WMS crossing-points. The resultant axially-stacked image can be expressed by

$$\boldsymbol{A} = \left\{ a_{l,i} \middle| a_{l,i} = \frac{1}{B}\sum_{k=ldk}^{ldk+B-1} c_k^i \quad \begin{matrix} l = \{1,2,\ldots,M\} \\ i = \{1,2,\ldots,Q\} \end{matrix} \right\} \tag{20}$$

where, $i$ is the frame number of gas concentraion set in total $Q$ frames and $l$ is the row number in total $M$ rows of a tomogram. $ldk$ is the starting index number of selected pixels or crossing-points in l-th row of a tomogram. $B$ is the number of columns to be averaged in each row of tomogram. An example of generating an axially-stacked sliced image $\boldsymbol{A}$ with respect to the time interval $[t_1, t_Q]$ is illustrated in figure 3, where the data in two central columns of each cross-sectional tomogram are extracted, and then the data of each row are averaged to approximately represent the spatial information, and the spatial information of $Q$ frames are sequentially stacked to generated the axially-stacked sliced image. It is worth noting that this work focuses on the visualisation of distinctive large bubble in pipeline, including the axial and radial information of the large bubble.

As illustrated in section 2.1, the optimal threshold $x^i$ for each concentration tomogram $\boldsymbol{C^i}$ is accurately determined by applying the size projection algorithm. Then the axially-stacked sliced image $\boldsymbol{A}$ can be binarised as a binary image $\widehat{\boldsymbol{A}}$ by following

$$a_{l,i} = \begin{cases} 0.0 & a_{l,i} < x^i \\ 1.0 & a_{l,i} \geq x^i \end{cases} \tag{21}$$

Here, the 0-1 interface in axially-stacked sliced image represent the gas-water interface between large bubbles and continuous water phase.

## 3. Simulation

### 3.1 Simulation setup

In order to investigate the performance of multistep image segmentation for imaging large bubble, sequences of images were reconstructed and compared from COMSOL simulation data. Based on the cross-sectional configurations of typical pipeline flow regimes, four sequences of setups were simulated to demonstrate the accuracy of size projection algorithm on (a) the water phase level of stratified setups, (b) the position of a single bubble setups, (c) the bubble size of a single bubble setups, (d) the bubble shape of a single bubble setups, which are given in figure 4(a)~(d).

Here, the background phase is tap water ($0.35\ mS/\ cm$), and the disperse phase is air ($0\ mS/\ cm$). The boundary was

Accepted Manuscript

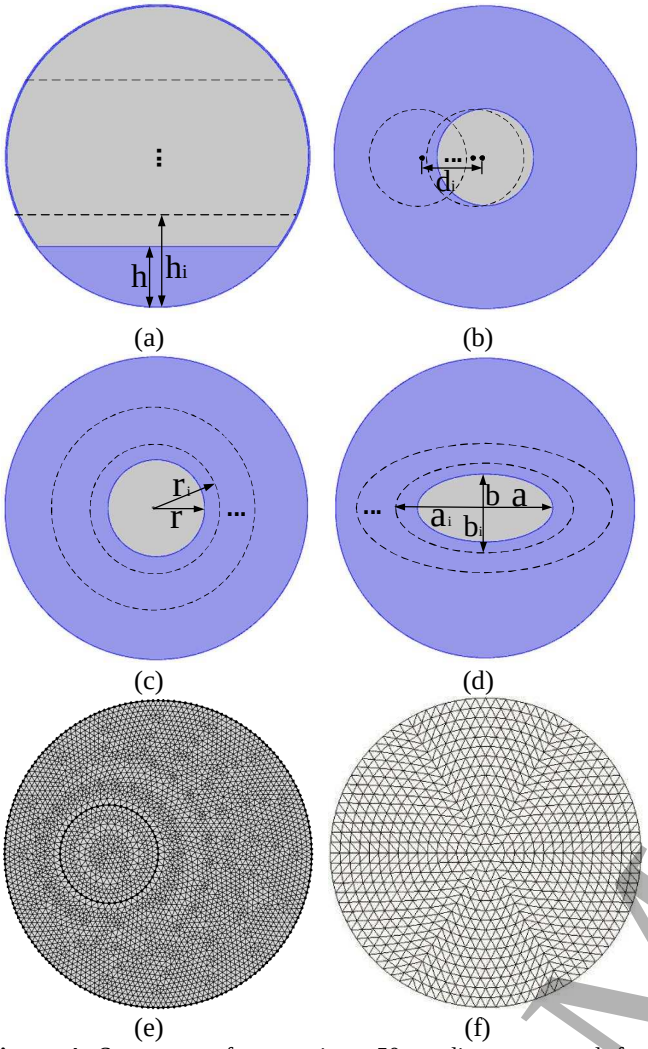


**Figure 4**. Sequences of setups in a 50mm-diameter vessel for COMSOL simulations (the grey and blue colour represent the gas phase and water phase) and FEM meshes. (a) Setups in regard to different water levels in horizontal pipe (level range: h=10~40mm). (b) Setups in different offsets of a size-fixed bubble (16mm in diameter) from centre to the wall (offset range: d=0~10mm). (c) Setups in different sizes of a centralised bubble (size range: r=5~15mm). (d) Setups in oval shape (a/b=2) having a same total area with round one of setups (c). (e) FEM mesh with 6612 elements having 176 boundary nodes for forward solution in COMSOL simulation. (f) FEM mesh with 1536 triangular pixels having 96 boundary nodes for inverse solution.

set as electrically insulated and zero initial potential. A pair of current terminals were employed for injecting current into and out of the sensing field. Then the default FEM forward solver in COMSOL Multiphysics 5.3a [33] was used to compute the simulation boundary voltages under an ultra-fine mesh. For example, one of setups (b) was meshed as 6612 elements having 176 boundary nodes, as shown in figure 4(e). In the simulation, a typical 16-electrode ERT sensor and adjacent sensing strategy were employed, which could generate 104 independent voltages for solving inverse problem.

Considering the importance of sensitivity back-projection (SBP) algorithm [34] in current applications, the SBP was employed for image reconstruction. Based on the reconstructed results of SBP, the proposed size projection algorithm was employed for image segmentation to extract the interface between the gas bubble and water. The processes of image reconstruction and segmentation were conducted under a mesh with 1536 triangular pixels having 96 boundary nodes, as shown in figure 4 (f).

In order to quantitatively assess the imaging results, relative image error (IE) [35], as expressed by equation (22), was employed to evaluate the imaging errors of SBP reconstruction algorithm and size projection algorithm.

$$IE = \frac{\|\hat{\boldsymbol{\sigma}} - \boldsymbol{\sigma}'\|}{\|\boldsymbol{\sigma}'\|} \qquad (22)$$

where, $\boldsymbol{\sigma}'$ is the conductivity vector of true setup, and $\hat{\boldsymbol{\sigma}}$ is the conductivity vector of reconstructed or segmented image.

## 3.2 Universality

In order to verify the universality of the proposed approach, typical setups of large bubbles in pipeline were investigated, and size projection algorithm binarised the SBP reconstructed images and extracted the size of large bubbles. Imaging errors of reconstructed algorithm and size projection algorithm are compared in figure 5~8, which clearly show that the errors of segmented images are lower than that of reconstructed images, that is, the proposed approach can greatly reduce the relative image errors (IEs) on all typical setups in figure 4(a)~(d).

For the setups of different levels of water phase in a horizontal pipe, as shown in figure 5, the two errors reach the lowest error at around half-pipe of water, while they turned larger at almost full-pipe or empty-pipe of water. For the setups in different positions of a size-fixed bubble from the centre to the wall, as shown in figure 6, the two errors have an increasing trend with the bubble shifting from the centre to the wall, but the error of segmented image is smaller one. For the setups in different sizes of a central bubble, as shown in figure 7, the error of segmented image is quite smaller than that of reconstructed image, and it keeps around 5% even the reconstructed image error has an increasing trend with bubble size increasing. For the setups in oval shape bubble having the same total areas of the round shape bubble setups at the centre of pipe, as shown in figure 8, the two errors of oval-shape setups are higher than the round-shape setups, and have an increasing trend with the increasing of bubble size.

## 3.3 Accuracy

The accuracy of proposed approach was investigated, and compared with common image segmentation methods, e.g. the fixed-value thresholding method [7] and histogram-based method [14]. Two setups in figure 4 were chosen for the comparison, i.e. (1) a round shape bubble with 5mm-offset from the centre of pipe, where the bubble diameter is 16mm,

Accepted Manuscript

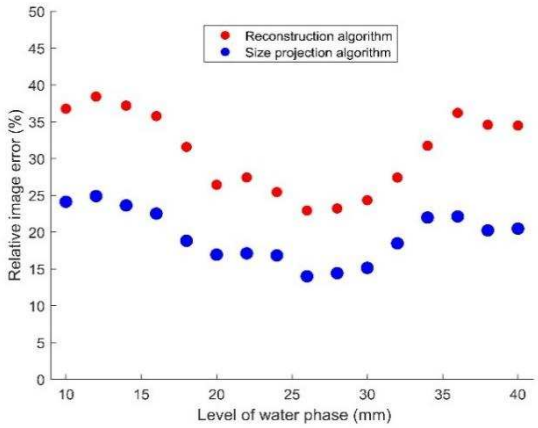


**Figure 5**. Relative image errors of the setups in different water levels in horizontal pipe (Mean image error of reconstruction algorithm is 30.9% and mean image error of size projection algorithm is 19.5%).

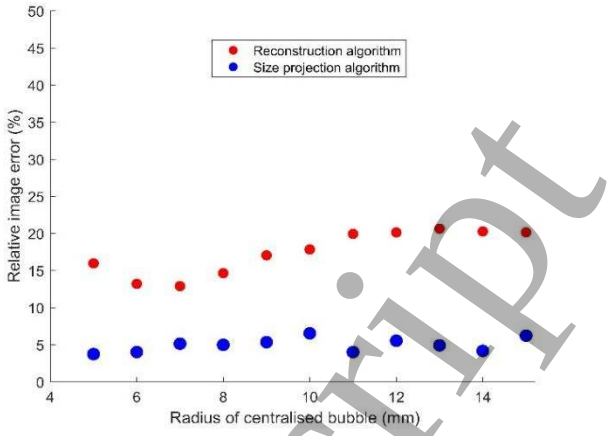


**Figure 7**. Relative image errors of the setups in different sizes of a central bubble (Mean image error of reconstruction algorithm is 17.5% and mean image error of size projection algorithm is 4.9%).

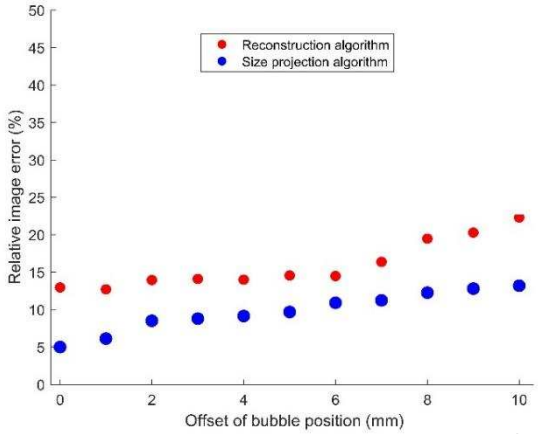


**Figure 6**. Relative image errors of the setups in different positions of a size-fixed bubble from centre to the wall (Mean image error of reconstruction algorithm is 15.9% and mean image error of size projection algorithm is 9.8%).

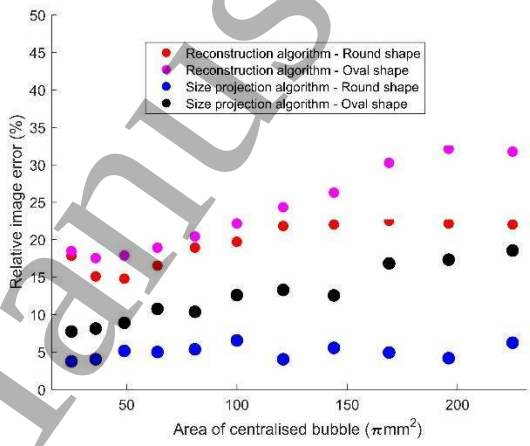


**Figure 8**. Relative image errors of the setups in round bubble and oval bubble with same total areas at the centre of pipe (Mean image error of reconstruction algorithm of oval setups is 23.6% and mean image error of size projection algorithm of oval setups is 12.4%).

**Table 1**. The relative image errors (IEs) of segmented images from different methods.

| Images | Setup-(1) | Setup-(2) |
|---|---|---|
| Reconstructed image of SBP | 14.55% | 18.92% |
| Segmented image from fixed-value (0.4) thresholding method [7] | 14.73% | 14.35% |
| Segmented image from histogram-based method (Ostu method [14]) | 15.99% | 17.78% |
| Segmented image from the proposed method | 9.67% | 10.75% |

and (2) an oval shape bubble at the centre of pipe, where the area of bubble is $64\pi\ mm^2$ and the ratio of the short axis to the long axis is ½. The three image segmentation methods were employed on the SBP reconstructed images of the two setups, and the results are compared in table 1. Comparing with the common image segmentation methods, the relative image errors of the proposed method are smallest, that is, the proposed method has a better performance for image segmentation.

**Table 2**. Time consumption of image segmentation methods.

| Images segmentation method | Searching Steps | Time |
|---|---|---|
| Fixed-value thresholding method | | 6.8 ms |
| Histogram-based method | 5 | 85 ms |
| The proposed method | 5 | 1232 ms |

## 3.4 Time consumption

The time expenses of image segmentation algorithms were tested by an Acer laptop with a 3.2GHz A10-7300 processor and a 4G running memory. The programs and all associated libraries (e.g. Mesh generator, Sensitivity matrix calculator, CG for forward solution, and GS for searching the best thresholding value, etc.) were coded and run in MATLAB software. For a better evaluation, the time expense of SBP for inverse solution was also tested as reference, which costed 26.32ms. Results are shown in table 2. Based on the reconstructed image of SBP, the fixed-value thresholding method directly gives the segmented image with a fixed time,.

Accepted Manuscript

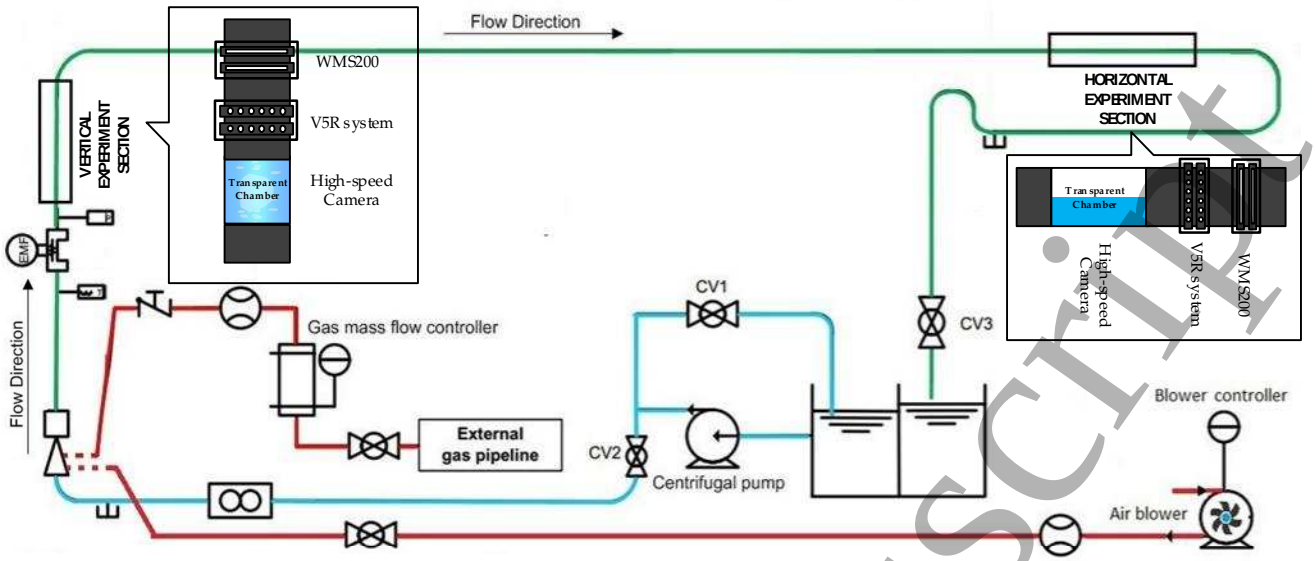


**Figure 9**. Sketch of gas-water flow loop facility in University of Leeds [38]. The red line, blue line and green line are the flowing routes with respect to single gas phase, single water phase, and the mixed fluids.

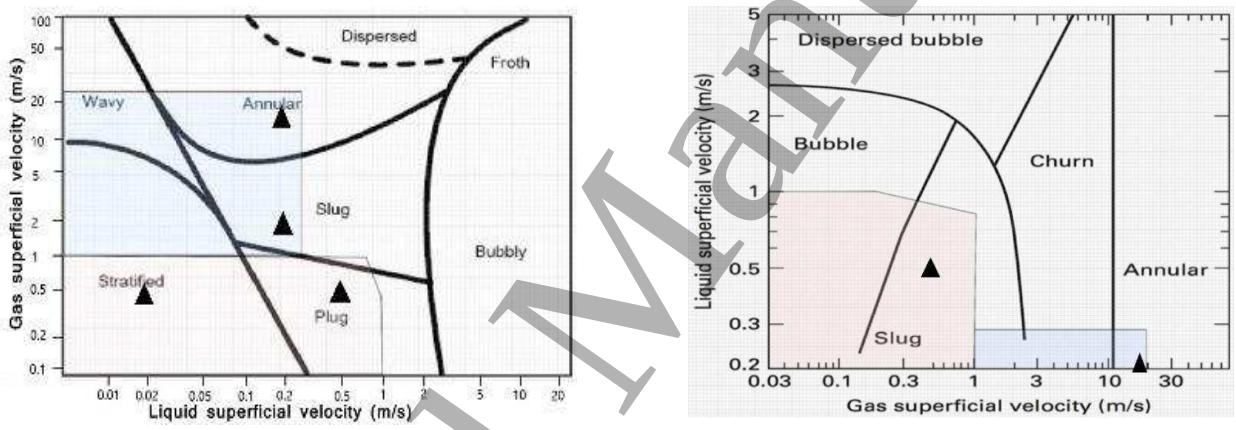


(a) (b)

**Figure 10**. Flow regime maps of OLIL flow loop [38]. (a) Horizontal flow regime map. (b) Vertical flow regime map. The triangles represent selected test points.

and the histogram-based method needs several searching steps to reach its "best" segmented image. The speed of proposed method is much slower than that of common methods, which is the product of solving forward solution in each searching steps.

From the perspective of imaging a distinctive large bubble, the proposed approach enhances the ERT visualisation performance of large bubble by removing the artifacts in reconstructed images. Comparing with other common image segmentation methods, the accuracy of imaging large bubble is greatly improved, which indicates the proposed approach can image the large bubble more accurately.

## 4. Experiments

### 4.1 Experimental setup

Gas-water flow in both horizontal and vertical pipelines were conducted to achieve different flow regimes for the evaluation of the proposed method. Figure 9 gives the sketch of the gas-water flow loop facility in Online instrumentation laboratory (OLIL) at University of Leeds, where the pipeline is made of PVC tubes with an internal diameter of 50mm. On both horizontal and vertical test sections, the instruments were arranged in the same order, that is the pipeline fluid flows through a transparent chamber, a ERT sensor and a WMS sensor, as depicted in the subfigures of figure 9. The V5R ERT system [36] with 312.5 dual frames per second (dfps) sampling speed and WMS200 system [37] with 5000 dfps sampling speed were utilised to collect flow data. Meanwhile, a high-speed camera was also installed to record the flow structures through a transparent chamber for comparison.

Accepted Manuscript

**Table 3**. Flow conditions of typical flow regimes

| Pipe Direction | $v_{Sg}(m/s)$ | $v_{Sw}(m/s)$ | GVF(%) | Observed regimes |
|---|---|---|---|---|
| Horizontal | 0.47 | 0.02 | 95.9 | Stratified flow |
| Horizontal | 0.51 | 0.50 | 50.5 | Plug flow |
| Horizontal | 2.06 | 0.20 | 81.2 | Slug flow |
| Horizontal | 17.00 | 0.20 | 98.8 | Annular flow |
| Vertical | 0.50 | 0.50 | 50.0 | Slug flow |
| Vertical | 18.42 | 0.20 | 98.9 | Annular flow |

In the experiments, the conductivities of gas and water phases were assumed as in $0\,mS/cm$ and $0.35\,mS/cm$ respectively. The gas flowrate was regulated from 0.0 to $1.0m/s$ by a gas mass flow controller (FMA5400, OMEGA) or from $1.0m/s$ to $20.0m/s$ by a frequency-controlled air blower (X1.32-3.0T, italBLOWERS). The water flowrate was manually controlled by a flow divider (V1 and V2) and driven by a centrifugal pump (NEMP300/20), where the water superficial velocity can be set from $0.0m/s$ to $1.0m/s$. According to the horizontal flow regime map (figure 10(a)) and vertical flow regime map (figure 10(b)) of OLIL flow loop, several tested points were selected for generating typical flow regimes, including stratified, plug, slug and annular regimes in horizontal pipeline and slug and annular regimes in vertical pipeline. The detailed information with respect to selected flow conditions are listed in table 3.

## 4.2 Visualisation results

Figure 11 and figure 12 show the visualisation results of typical flow regimes, where each axially-stacked ERT images consist of 625 frames of concentration data with a time length in 2 seconds and all images of WMS consist of 10000 frames of concentration data with the same time length. The visualisation results were rendered by a conventional colour mapping method, where the red represents the gas and the blue represents the water. In each set of figures, the four images are produced by concatenating several consecutive screenshots of videos from the high-speed camera, the original concentration data collected by WMS system, the original concentration data collected by ERT system, and the binary ERT concentration data obtained from the proposed method (SPA), respectively. Here, the camera-recorded image was given to the operator a direct visual reference for understanding the flow conditions, and the WMS image was provided as a relatively accurate reference for the comparison of ERT and SPA images since WMS is possible a most convenient and intrusive imaging facility [31].

In order to better representation of flow visualisation, the average gas local velocity $\overline{v_g}$ is estimated based by the aforementioned online cross-correlation method or the superficial gas velocity when the method is not inapplicable. However, the velocity calculation is based on the WMS system since the ERT (V5R) system in the use did not achieve the required sampling rate for cross-correlated velocity calculation [29] in the work. And the fluid travel distance $Dist$ can be derived by

$$Dist = \overline{v_g} \cdot N_t / DAS \quad (23)$$

where, $N_t$ is the total number of frames for stacked images, and $DAS$ is the data acquisition speed of WMS system.

For a horizontal stratified flow, as shown in figure 11(a), all images clearly reveal that the gas and water phases are separately flowing at the top part and bottom part of the pipe. The SPA image shows the clearly sharp gas-water interface, while the conventional ERT and WMS images only show the blurry gas-water interface. For the horizontal plug and slug flow, as shown in figure 11(b) and (c), all images clearly reveal that the gas phase is deformed into large bubbles (i.e. gas plugs or slugs) at the top of the pipe and some small bubbles exist between gas plugs or slugs. However, only SPA image shows a clear boundary of large bubble. The situation changes when comes to a horizontal annular flow, as shown in figure 11(d), the camera-recorded image and WMS image show similar results, i.e. the gas phase is flowing at the centre of pipe with being surrounded by a thin water film. The ERT image shows a thin water film at the bottom, but does not show the thin water film at the top. The SPA image shows clear gas-water interface between the centre gas and the bottom water, and also does not show the thin water film at the top. The reason is that the top water film is too thin to be identified by ERT system with SBP reconstruction algorithm.

For a vertical slug flow, as shown in figure 12(a), the camera-recorded image reveals that the slug bubbles have nearly the same cross-section of the pipe and some small bubbles exist at their tails. The WMS image shows similar results, with identifying bullet shape of slug bubbles. The ERT image only shows the bullet-shaped and blurry boundary of the slug bubble, while the SPA image shows a clear slug bubble boundary. For a vertical annular flow, as shown in figure 12(b), all images reveal that a gas core flows at the centre of pipe with being surrounded by an annular water film, but only the SPA image shows the gas core with clear gas-water interface.

From the perspective of imaging a distinctive large bubble, the large bubbles in each flow regime are clearly identified with sharp bubble boundary by the proposed method, and the visualisation results of large bubbles are kept a high consistency between different methods. Unfortunately, the small bubbles are incapable to be identified since the proposed method assumed ignoring the influence of small bubbles.

## 4.3 Quantitative evaluation

In order to quantitatively evaluate the proposed method, three cross-sectional images at different positions of the plug flow (figure 11c) are selected for quantitative comparison of WMS, ERT and SPA results. They are (1) only a large bubble, (2) the tail of large bubble with some small bubbles, and (3) few small bubbles in the cross-sections. Since the format of camera-.

Accepted Manuscript

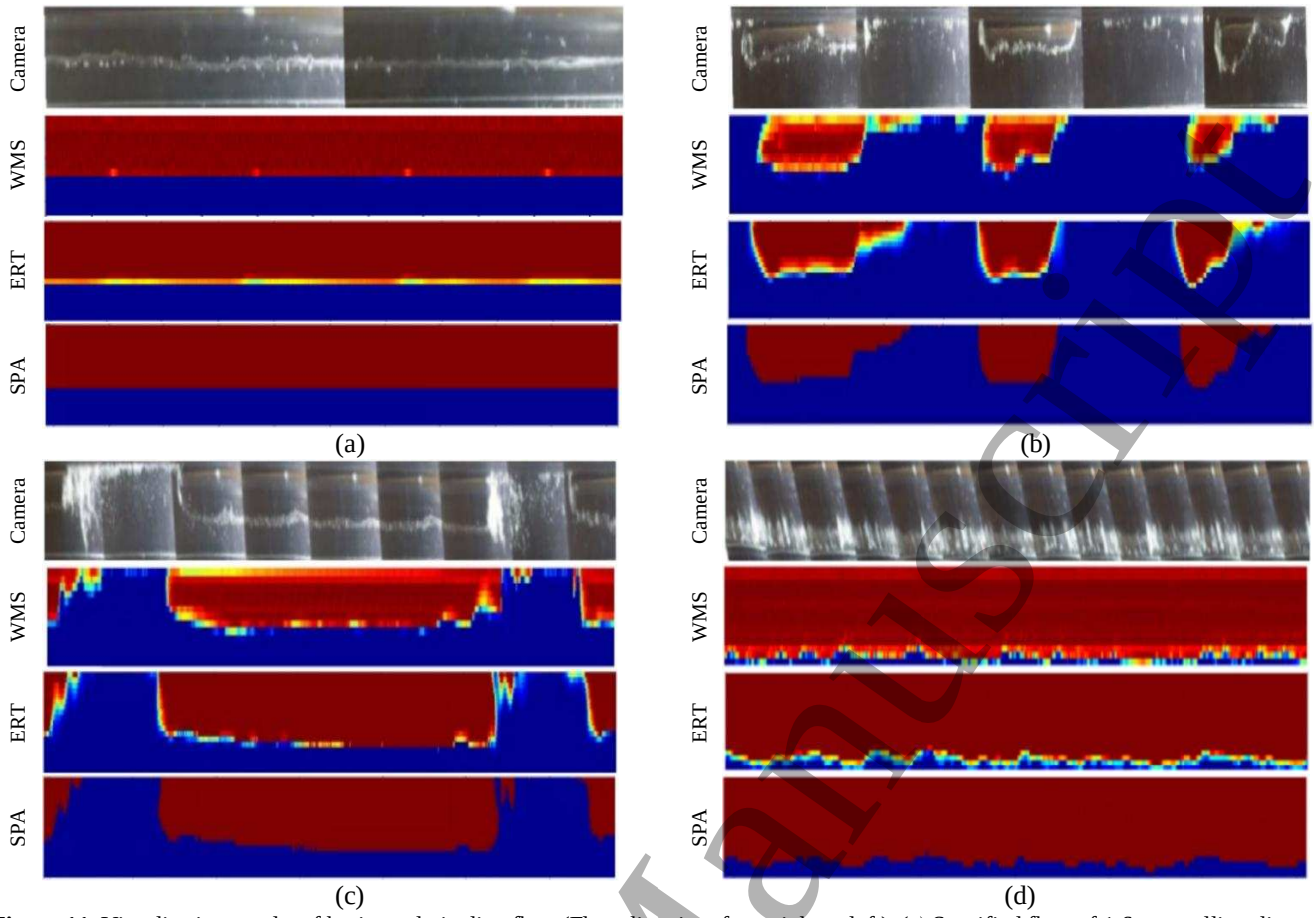


**Figure 11**. Visualisation results of horizontal pipeline flow (Flow direction: from right to left). (a) Stratified flow of 1.6m travelling distance ($v_{Sg}$=0.47m/s, $v_{Sw}$=0.02m/s). (b) Plug flow of 3.3m travelling distance ($v_{Sg}$=0.51m/s, $v_{Sw}$=0.5m/s). (c) Slug flow of 7.7m travelling distance ($v_{Sg}$=2.06m/s, $v_{Sw}$=0.2m/s). ). (d) Annular flow of 37m travelling distance ($v_{Sg}$=17m/s, $v_{Sw}$=0.2m/s).

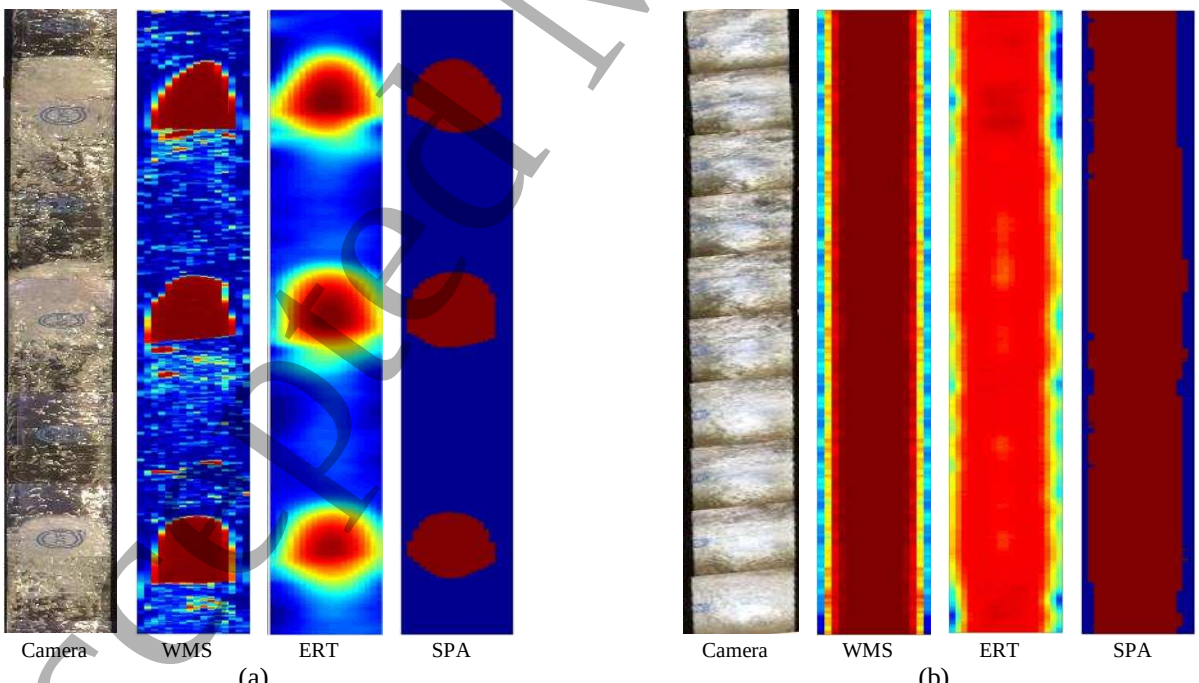


**Figure 12**. Visualisation results of vertical pipeline flow (Flow direction: from bottom to top). (a) Slug flow of 3.1m travelling distance ($v_{Sg}$=0.5m/s, $v_{Sw}$=0.5m/s). ). (b) Annular flow of 46m travelling distance ($v_{Sg}$=18.42m/s, $v_{Sw}$=0.2m/s).

Accepted Manuscript

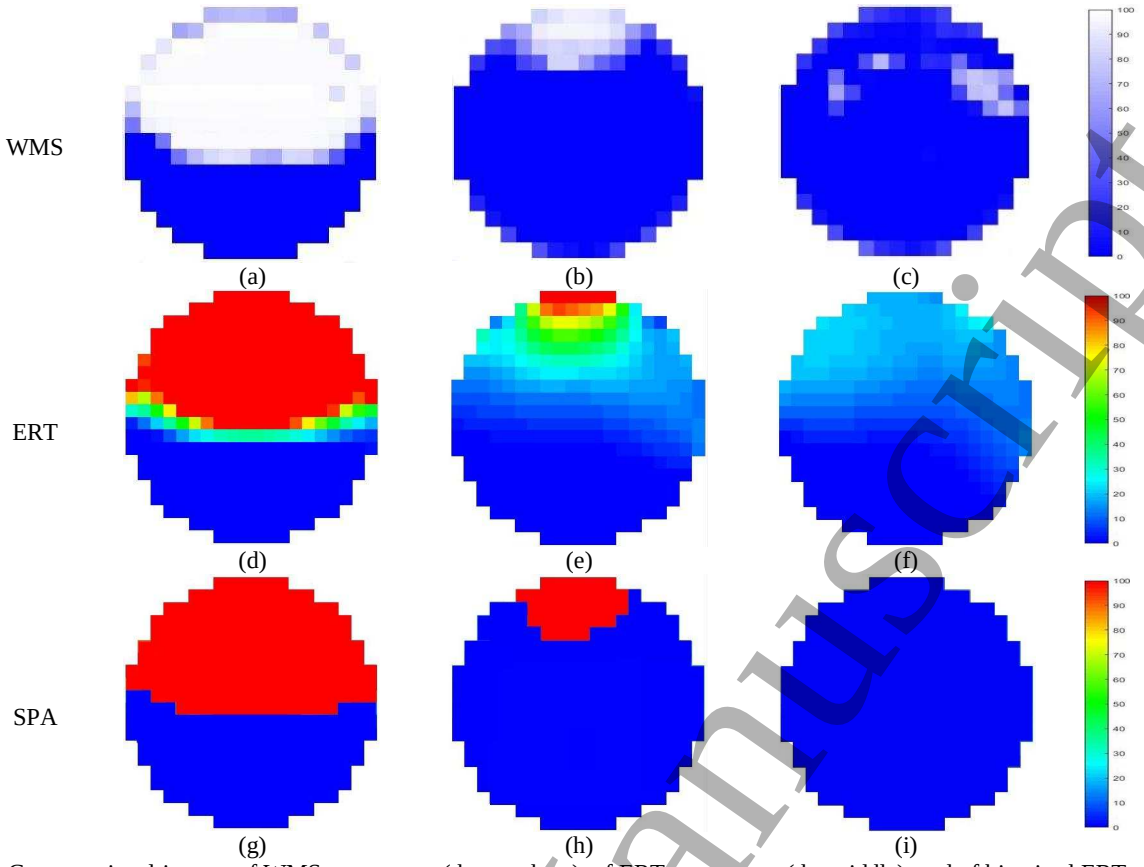


**Figure 13**. Cross-sectional images of WMS tomograms (the top three), of ERT tomograms (the middle), and of binarised ERT tomograms by SPA (the bottom). (a), (d) and (g) are for only a large bubble; (b), (e) and (h) are for the tail of large bubble with some small bubbles; (c), (f) and (i) are for few small bubbles in the cross-sections of horizontal plug flow.

**Table 4**. Mean gas concentrations of selected cross-sectional images

| Methods | Case (1) | Case (2) | Case (3) |
|---|---|---|---|
| WMS | 52.60% | 13.79% | 5.67% |
| ERT | 53.77% | 14.19% | 7.09% |
| SPA | 54.74% | 10.76% | 0% |

recorded image is not the same as the cross-sectional image of tomogram, and the quality of photography of flow patterns is greatly affected by the transparency and overlap effect of bubbles, it is rather challenging to quantitatively represent the bubbles in camera-recorded image. Therefore, only the other three methods are quantitatively compared in this work. The comparison results are shown in figure 13, and their mean gas concentrations are compared in table 4.

For only a large bubble existing, the WMS image and ERT image (figure 13a and figure 13d) show similar results, i.e. a large bubble with blurry boundary, while the SPA image (figure 13g) shows sharp bubble boundary. The mean gas concentrations of three methods are very close. For the tail of plug bubble with some small bubbles, the situation of cross-sectional images does not change, but the mean gas concentration of SPA result tends to underestimate it. This is mainly because the contribution of small bubbles is attributed to the large bubble. When there are only few small bubbles, the WMS image and ERT image (figure 13c and figure 13f) shows an approximate gas phase distribution, while the SPA image (figure 13i) only shows water phase, and the mean gas concentration of SPA result is 0%. This is the product of the assumption that the effect of small bubbles is ignoring.

## 4. Conclusions

A size projection algorithm was proposed to enhance the quality of ERT visualisation on gas-water two-phase flows, which focuses on imaging the distinctive large bubbles with sharp boundary. The simulation results demonstrated the effectiveness of gas-water interface extraction. The visualisation results are also compared with the WMS image and camera-recorded video, presenting a high consistency between them. The proposed method is actually an optimal threshold based method which overcomes the challenge from the determination of the thresholding value in use of the empirical thresholds and low robustness of histogram-based models.

However, few aspects still require more efforts. Firstly, the imported ERT concentration sets need to be reconstructed with suitable tomographic algorithms since the accuracy of proposed method highly relies on the reconstruction accuracy. For example, SBP algorithm has a certain limitation on

Accepted Manuscript

vertical annular flow if the water film is too thin. Secondly, the proposed method relies on the distinguishability of inverse solution, that is, the proposed method might give different results based on differently reconstructed images. For the cases of multiple bubbles, the proposed method based on the higher-resolution reconstructed image has better suitability of imaging multiple bubbles. However, the multiple bubbles are combined into a larger bubble by SBP algorithm in most cases. Thirdly, due to the limited resolution of ERT, the disperse small bubbles is hardly identified and is mixed in the reconstructed artifacts of the existing large bubble, which would put the contribution of disperse small bubbles on the large bubble in the proposed method. Fourthly, too much time consumption is caused by many threshold-searching steps since GS method is a linear convergence method. The time consumption could be relieved by employing efficient line search methods, e.g. Newton or parabolic method.

## Acknowledgements

The authors would like to express their gratitude for the support from the Chinese Scholarship Council (CSC) and the School of Chemical and Process Engineering, who made Mr. Li's study at the University of Leeds possible.

## Appendix

### A.1 Process of GS method

The process of GS method for best threshold selection by minimising the projection error in this paper is given below:

**Step 1:** Determine the threshold region $[x_L, x_H]$, minimum convergence error $\varepsilon > 0$, and maximum steps $P$.

**Step 2:** Let $p = 0$. Calculate the initial thresholding tentative value $x_0 = (x_L + x_H)/2$, and the initial projection error $\boldsymbol{e}(x_0)$.

**Step 3:** If $\|\boldsymbol{e}\|_2 \leq \varepsilon$ or $p > P$, stop and export the corresponding threshold $x$. Otherwise, go to step 4.

**Step 4:** Calculate left and right thresholding tentative values $x_1 = x_L + 0.382(x_H - x_L)$, $x_2 = x_L + 0.618(x_H - x_L)$, and the corresponding projection errors $\boldsymbol{e}(x_1)$, $\boldsymbol{e}(x_2)$. Let $p = p + 1$.

**Step 5:** If $\|\boldsymbol{e}(x_1)\|_2 \leq \|\boldsymbol{e}(x_2)\|_2$, go to step 6. Otherwise, go to step 7.

**Step 6:** Let $x_0 = x_1$, $\boldsymbol{e}(x_0) = \boldsymbol{e}(x_1)$, and $x_H = x_2$. Go to step 3.

**Step 7:** Let $x_0 = x_2$, $\boldsymbol{e}(x_0) = \boldsymbol{e}(x_2)$, and $x_L = x_1$. Go to step 3.

## References

[1] Levy S 1999 Two-phase Flow in Complex Systems 1st ed (Wiley-Interscience)

[2] Wang M 2015 Industrial Tomography: Systems and Applications 1st ed (Woodhead Publishing)

[3] Rajan V S V, Ridley R K and Rafa K G 1993 Multiphase flow measurement techniques-a review Journal of Energy Resources Technology **115** 151-161

[4] Boyer C, Duquenne A M and Wild G 2003 Measuring techniques in gas-liquid and gas-liquid-solid reactors Chem Eng. Sci. **57** 3185-3215

[5] Baker R C 2000 Flow Measurement Handbook: Industrial Designs, Operating Principles, Performance, and Applications 1st ed (Cambridge University Press)

[6] Wang M, Ma Y, Holliday N, Dai Y, Williams R A and Lucas G 2005 A high-performance EIT system IEEE Sens. J. **5** 289-299

[7] Wang M, Dickin F J and Williams R A 1995 A study on cyclonic separators using electrical impedance tomography Proc. 2nd International Conference on Multiphase Flow Kyoto, Japan

[8] Wang M, Dickin F J and Williams R A 1995 Air core definition in LARCODEMS separators using electrical resistance tomography. Proc. International Symposium on Measuring Techniques for Multiphase Flows, Nanjing, China

[9] Xie C G 1992 Electrical capacitance tomography for flow imaging: system model for development of image reconstruction algorithms and design of primary sensors. Circuits Devices & Systems Iee Proceedings G **139** 89-98

[10] Yan Y, Liu L J, Xu Hand Shao F Q 2001 Image reconstruction in electrical capacitance tomography using multiple linear regression and regularization Meas. Sci. Technol. **12** 575

[11] Glasbey C A 1993 An Analysis of Histogram-Based Thresholding Algorithms Graphical Models and Image Processing **55** 532-537

[12] Bankman I N 2009 Handbook of Medical Image Processing and Analysis (Elsevier)

[13] Lai C and Tseng D 2005 A hybrid approach using Gaussian smoothing and genetic algorithm for multilevel thresholding International Journal of Hybrid Intelligent Systems **1** 143-152

[14] Otsu N 1979 A threshold selection method from gray-level histograms. IEEE T Syst. Man Cy-S 9 62-66

[15] Kim B S, Khambampati A K, Kim S and Kim K Y 2011 Image reconstruction with an adaptive threshold technique in electrical resistance tomography Meas. Sci. Technol. **22** 104009

[16] HEWITT G F 1970 Annular Two-phase Flow 1st ed (Pergamon)

[17] Luo X, Lee D J, Lau R, Yang G and Fan L S 1999 Maximum stable bubble size and gas holdup in high-pressure slurry bubble columns Fluid Mechanics and Transport Phenomena **45** 665-680

[18] Razzaque M M 2005 Bubble size distribution in a large diameter pipeline Proc. 5th IMEC & 10th APM Dhaka

[19] Jia J, Wang M and Faraj Y 2015 Evaluation of EIT systems and algorithms for handling full void fraction range in two-phase flow measurement Meas. Sci. Technol. **26** 015305.

[20] Wang M 2002 Inverse solutions for electrical impedance tomography based on conjugate gradients methods Meas. Sci. Technol. **13** 101-117

[21] Wang M 1999 Three-dimensional effects in electrical resistance tomography Proc. 1st World Congress on Industrial Process Tomography Buxton, UK

[22] Murai T and Kagawa Y 1985 Electrical impedance computed tomography based on a finite element model IEEE Trans. Biomed. Eng. **32** 177-184

Accepted Manuscript

[23] Yorkey T J, Webster J G and Tompkins W J 1987 Comparing reconstruction algorithm for electrical impedance tomography. IEEE Trans. Biomed. Eng. **34** 843–51

[24] Abdullah M Z 1993 Electrical impedance tomography for imaging conducting mixture in hydrocyclone separators PhD Thesis. UMIST

[25] Pronzato L 1998 A generalized golden-section algorithm for line search. IMA J. Math. Control I. **15** 185-214

[26] MOSAIC Scientific Ltd. 2009 AIMFlow Standard Version 1.0 User Manual, AIMFlow Manual Leeds, UK

[27] Wang Q, Jia X, Wang M 2019 Bubble mapping: Three-dimensional visualisation of gas-liquid flow regimes using electrical tomography. Meas. Sci. Technol.

[28] Wang M, Jia J, Faraj Y, Wang Q, Xie C, Oddie G, Primrose K, Qiu C 2015 A new visualisation and measurement technology for water continuous multiphase flows Flow Meas. Instrum. **46** B204-212

[29] Wang M, Ma Y, Holliday N, Dai Y, Williams R A, Lucas G 2005 A high-performance EIT system. IEEE Sensors Journal **5** 289-299

[30] Beyer M, Szalinski L, Schleicher E and Schunk C 2018 Wire-Mesh Sensor Data Processing Software User Manual and Software Description User's Manual Version 1.3 Dresden, Germany

[31] Prasser H M, Misawa M, Tiseanu I 2005 Comparison between wire-mesh sensor and ultra-fast x-ray tomography for an air-water flow in a vertical pipe Flow Meas. Instrum. **16** 73-83

[32] Olerni C, Jia J, Wang M 2013 Measurement of air distribution and void fraction of an upwards air-water flow using electrical resistance tomography and a wire-mesh sensor Meas. Sci. Technol. **24** 035403

[33] COMSOL Inc. 2018 COMSOL Multiphysics Reference Manual Version 5.3a Stockholm, Sweden

[34] Kotre C J 1994 EIT image reconstruction using sensitivity weighted filtered back-projection Physiol. Meas. **15** A125-36

[35] Yang W, Peng L 2002 Image reconstruction algorithms for electrical capacitance tomography Meas. Sci. Technol. **14** R1-R13

[36] Jia J, Wang M, Schlaberg H I and Li H 2010 A novel tomographic sensing system for high electrically conductive multiphase flow measurement Flow Meas. Instrum. **21** 184–90

[37] Teletronic Rossendorf GmbH 2015 Wire Mesh Sensor System WMS200 Manual Version 1.7 Radeberg, Germany

[38] Jiri P 2016 Air-water Loop Operation Procedures User's Manual Version 2.0 Leeds, UK

Accepted Manuscript